Thermobaric Convection

by

Roland W. Garwood, Jr., Shirley M. Isakari
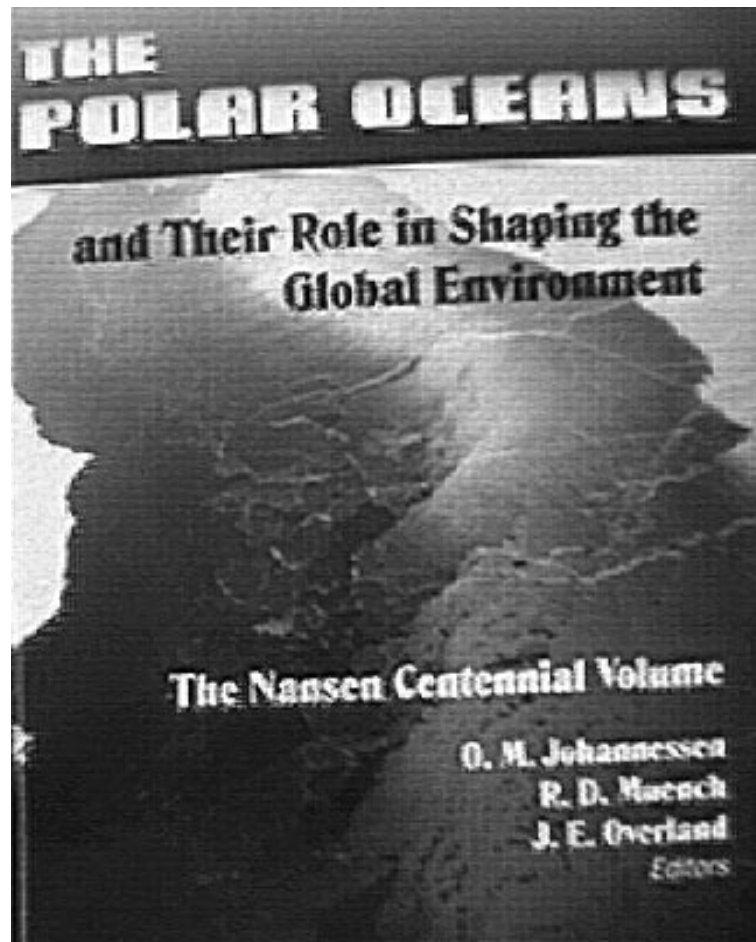
Naval Postgraduate School, Monterey, California, USA

and

Patrick C. Gallacher

NRL, Stennis Space Center, Mississippi, USA

in Geophysical Monograph 85:

Thermobaric Convection

Roland W. Garwood, Jr., Shirley M. Isakari

Naval Postgraduate School, Monterey, California, USA

and

Patrick C. Gallacher

NRL, Stennis Space Center, Mississippi, USA

Large-eddy simulation of two cases of free convection in the polar seas reveal the three-dimensional structure of thermobaric-enhanced turbulence, with and without salinity stratification. In the first case, with no initial stratification, 3.6 km-deep free thermal convection produces anticyclonic cells of rising warmer water at the surface, with largest cell diameters of about 1 km. Narrow linear shear zones of colder near-surface water between these warm cells are the source of sinking cyclonic thermobaric plumes that provide the energy to power the convective system. The prediction of a mid-depth maximum in the turbulent kinetic energy caused by thermobaricity is corroborated numerically. In the second case, thermal convection in a mixed layer overlying salinity-stratified warmer water may generate two kinds of conditional instabilities. In a *thermobaric parcel instability*, detraining parcels of mixed-layer water may penetrate the pycnocline without significant mixing of the stable surrounding water. In a *thermobaric layer instability*, a nonturbulent layer may become statically unstable and turbulent if advected below a predicted critical depth. For either kind of instability, the thermobaric increase in density of a parcel or layer of cold water may cause plumes of near-surface water to penetrate deep into the pycnocline and possibly to the bottom as "cumulus towers" of the polar seas.

1. INTRODUCTION

The term "thermobaricity" was coined by McDougall [1984] and generally refers to phenomena related to the pressure dependence of the thermal expansion coefficient for the density (ρ) of seawater, $\alpha = -\rho^{-1}\frac{\partial \rho}{\partial T}$. The magnitude of α increases with pressure (p) and is approximated by the first two terms of a Taylor series expansion in p,

$$\alpha \cong \alpha_0\left(1 + \frac{p}{\rho_0 g H_\alpha}\right) \qquad (1)$$

where α_0 and ρ_0 are the surface values for thermal expansion and density, T is temperature, g is gravity, and H_α is the thermobaric depth scale,

$$H_\alpha = \alpha_0 \Big/ \frac{\partial \alpha}{\partial z}\bigg|_{z=0} , \qquad (2)$$

with the vertical coordinate (z) being positive up. For the coldest sea water H_α is about 900 m.

As first pointed out by Gill [1973] this nonlinearity in the equation of state should cause a cold plume of saline shelf water produced by freezing to experience an additional decrease in stability as it flows down-shelf if the potential temperature of the surrounding water exceeds that of the plume by a finite amount, $\delta\theta$. This buoyancy reduction (δb) with depth (z) is explained by the thermobaric term of (3) that reduces the static stability for finite vertical displacement, δz:

$$\delta b = \left(N^2 - \frac{\alpha_0 g \delta\theta}{H_\alpha}\right)\delta z \qquad (3)$$

where $N = (\alpha g \partial\theta/\partial z - \beta g \partial S/\partial z)^{1/2}$ is the buoyancy frequency for infinitesimal parcel displacement, and $\theta(z)$ and $S(z)$ are the ambient profiles of potential temperature and salinity.

A possible open-ocean role for thermobaricity was first considered by Killworth [1979], following the discoveries of chimneys in the Weddell [Gordon, 1978] and Iceland Seas [Foldvik, personal communication]. Killworth included thermobaricity in the calculation of hydrostatic stability for the Weddell Sea chimney. Farmer and Carmack

[1981] and Carmack and Farmer [1982] showed its importance in freshwater lakes. Although other deep convection numerical studies [Brugge et al., 1991; Jones and Marshall, 1993] have considered nonhydrostatic effects, none have included thermobaricity until recently [Garwood, 1991; 1993]. The dynamic nature of thermobaric instabilities seems to have been overlooked.

1.1. Dynamic Effects of Thermobaricity Hypothesized

Earlier mixed layer models for polar-sea application have not included thermobaricity either [e.g. Lemke, 1987; Martinson, 1990]. However, searching for mechanisms to explain deep mixed layer entrainment, Garwood [1991] showed a significant increase in the buoyancy flux (Figure 1) and in the predicted mixed layer entrainment rate when thermobaricity was included in the steady-state turbulent kinetic energy (TKE) budget. A mid-depth maximum in the TKE was predicted for the deepest polar sea free convection because of thermobaricity.
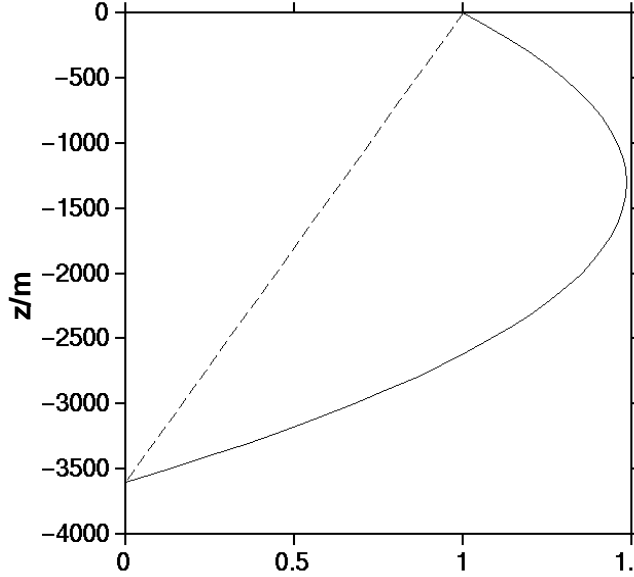

Fig. 1. Normalized buoyancy flux (solid) versus depth associated with a linear turbulent heat flux (dashed) in deep sea water with surface temperature near freezing [Garwood, 1991].

In spite of the enhanced mixed layer buoyancy flux, when salinity stratification is included, mixed layer physics can not explain recent small-scale deep convection observations. CTD sections by Rudels et al. [1989], towed thermistor chain observations reported by Scott and Killworth [1991], and moored thermistor/conductivity time series of Schott et al. [1993] provide compelling evidence of small scale vertical convection events with horizontal widths of order 2 km and less in the Iceland and Greenland Seas. None of these observations of vertical plumes included evidence of horizontal homogenization that would be predicted by traditional mixed layer physics.

To explain these plumes that extend below the surface mixed layer into the halocline, Garwood [1992a,b] has suggested that deep penetrative convection in the polar seas may have dynamic and thermodynamic similarities to atmospheric cumulus convection, in that buoyancy is not conserved in either system. Two kinds of oceanic conditional instabilities were hypothesized. These processes, a parcel instability and a layer instability, are analogous to atmospheric conditional instabilities of the first and second kind [Holton, 1972].

1.2. Large-Eddy Simulation (LES) to Numerically Test Hypotheses

A nonhydrostatic numerical model for high Reynolds number turbulent flow is used to test the above hypotheses. The LES model of Moeng [1984], which was adapted to shallow ocean mixing by McWilliams et al. [1992], was modified for application to oceanic deep convection by adding a prognostic equation for salinity and including the pressure dependence (1) in the equation of state. The Boussinesq equations plus heat and salinity budgets are used to explicitly calculate the three-dimensional large-eddy velocity, salinity, and potential temperature fields:

$$\frac{du}{dt} = -\frac{1}{\rho}\frac{\partial p}{\partial x} + fv - 2\Omega_y w +$$
$$\frac{\partial}{\partial x}\left(K_M\frac{\partial}{\partial x}u\right) + \frac{\partial}{\partial y}\left(K_M\frac{\partial}{\partial y}u\right) + \frac{\partial}{\partial z}\left(K_M\frac{\partial}{\partial z}u\right) \quad (4)$$

$$\frac{dv}{dt} = -\frac{1}{\rho}\frac{\partial p}{\partial y} - fu +$$
$$\frac{\partial}{\partial x}\left(K_M\frac{\partial}{\partial x}v\right) + \frac{\partial}{\partial y}\left(K_M\frac{\partial}{\partial y}v\right) + \frac{\partial}{\partial z}\left(K_M\frac{\partial}{\partial z}v\right) \quad (5)$$

$$\frac{dw}{dt} = -\frac{1}{\rho}\frac{\partial p}{\partial z} + \alpha g(\theta - \theta_0) + 2\Omega_y u +$$
$$\frac{\partial}{\partial x}\left(K_M\frac{\partial}{\partial x}w\right) + \frac{\partial}{\partial y}\left(K_M\frac{\partial}{\partial y}w\right) + \frac{\partial}{\partial z}\left(K_M\frac{\partial}{\partial z}w\right) \quad (6)$$

$$\frac{\partial}{\partial x}u + \frac{\partial}{\partial y}v + \frac{\partial}{\partial z}w = 0 \quad (7)$$

$$\frac{dS}{dt} = \frac{\partial}{\partial x}\left(K_S\frac{\partial}{\partial x}S\right) + \frac{\partial}{\partial y}\left(K_S\frac{\partial}{\partial y}S\right) + \frac{\partial}{\partial z}\left(K_S\frac{\partial}{\partial z}S\right) \quad (8)$$

$$\frac{d\theta}{dt} = \frac{\partial}{\partial x}\left(K_\theta\frac{\partial}{\partial x}\theta\right) + \frac{\partial}{\partial y}\left(K_\theta\frac{\partial}{\partial y}\theta\right) + \frac{\partial}{\partial z}\left(K_\theta\frac{\partial}{\partial z}\theta\right) \quad (9)$$

Here u, v and w are the easterly, northerly and vertical velocity components, f is the vertical Coriolis parameter, and

$2\Omega_y$ is the horizontal Coriolis parameter, and the total derivative is $\dfrac{d}{dt} = \dfrac{\partial}{\partial t} + u\dfrac{\partial}{\partial x} + v\dfrac{\partial}{\partial y} + w\dfrac{\partial}{\partial z}$.

The prognostic equations (4-9) for resolved scale momentum, salinity and potential temperature are solved using second order, centered finite differencing in the vertical and the pseudospectral method of Fox and Orszag [1973] in the horizontal. Time advancement is accomplished using the Adams-Bashforth scheme.

The subgrid scale fluxes are parameterized with eddy mixing coefficients ($K_{M,S,\theta}$) that are time- and space-dependent and calculated with second order turbulence closure, following Smagorinsky [1963], with

$$K_M = 0.1\lambda\sqrt{e} \qquad (10)$$

and

$$K_S = K_\theta = [1 + (2\lambda)/L]K_M \qquad (11)$$

The subgrid TKE length scale λ is equal to the grid scale L,

$$\lambda = L = (\Delta x \Delta y \Delta z)^{1/3} \qquad (12)$$

unless the stratification is stable, when it is

$$\lambda = \lambda_s = 0.76\sqrt{e}N \qquad (13)$$

if $\lambda_s < L$, where N is the buoyancy frequency, and e is the subgrid (unresolved) TKE. It is computed by

$$\frac{de}{dt} = K_M\left[\left(\frac{\partial u}{\partial z}\right)^2 + \left(\frac{\partial v}{\partial z}\right)^2\right]$$
$$-gK_\theta\left(\alpha\frac{\partial}{\partial z}\theta - \beta\frac{\partial}{\partial z}S\right) + \frac{\partial}{\partial z}\left(2K_M\frac{\partial e}{\partial z}\right) - \varepsilon \qquad (14)$$

where the four terms on the right of (14) are subgrid shear production, buoyancy flux, turbulent transport, and viscous dissipation. Subgrid dissipation (ε) is modeled as a function of the subgrid TKE,

$$\varepsilon = (0.19 + 0.51\lambda/L)e^{1.5}/\lambda \qquad (15)$$

More extensive details concerning the subgrid scale fluxes and the numerical method are provided by Moeng (1984).

For the first experiment the predicted eddy viscosity is on the order of 0.1 $m^2 s^{-1}$ or less, and the LES Reynolds number is of order 10^3 or larger. The pseudospectral method allows use of a high-wavenumber cutoff filter to define the resolved scales and to remove the small-scale noise without artificially damping the resolved scale motions [Moeng and Wyngaard, 1988]. Thus the high model Rey-

nolds number causes a robust turbulence spectrum to be achieved that has the correct -5/3 slope at high wavenumbers [Gallacher, 1990].

In the following sections, thermobaric convection is examined and numerically simulated, first for purely thermal free convection and then for conditional instabilities in which salinity stratification allows for the build up and subsequent release of thermobaric potential energy.
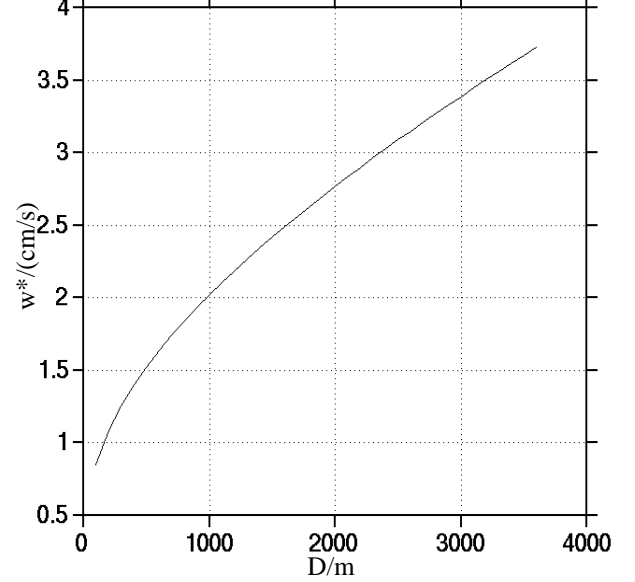

Fig. 2. Free convection velocity scale (w*) as a function of mixing depth (h) for a fixed value of surface heat flux, $Q_0 = 100$ watts/m^2.

2. THERMOBARIC FREE CONVECTION

To demonstrate the power magnification attributable to thermobaricity in the generation of turbulence, the vertical integral over the water column of the buoyancy flux is considered,

$$\frac{\text{Power}}{(\text{Area})\rho} = \int_{-h}^{\upsilon}(\alpha g\overline{\theta w} - \beta g\overline{Sw})dz \equiv \quad w^{*3}, \quad (16)$$

where h is mixed layer depth, overbars denote horizontal averages in a system that is approximately horizontally homogeneous in the mean, and w is the vertical turbulent velocity. The velocity scale w* that is defined by (4) is expected to be representative of the magnitude of the turbulent velocity present in the system at equilibrium when dissipation balances buoyant production, and storage of TKE is negligible. For no salinity flux, $\overline{Sw} = 0$, and a heat flux, $Q = \rho C_p\overline{\theta w}$, that decreases linearly from the surface value (Q_0) to zero at a depth z=-h, (1) and (4) yield

$$w* = \left\{ 0.5\alpha_0 gh \frac{Q_0}{\rho C_p}[1 + h/(3H_\alpha)] \right\}^{1/3} \quad , \quad (17)$$

where C_p=3990 J/Kg/C and ρ=1028 Kg/m^3 are representative mixed layer values for specific heat and density.

For typical surface winter polar sea conditions (Q_0 =200 watts/m^2; S=34.5, T(0)=- 1.8), Figure 2 shows that w* increases from 0.7 cm/sec for a convection depth h = 50 m to 2.4 cm/sec for h = 1500 m, and to more than 3.5 cm/sec if convection penetrates below 3500 m.

2.1. Large-Eddy-Simulation of Thermally-Driven Deep Free Convection Without Salinity

The first of two numerical experiments is for thermally-driven deep polar sea free convection, without salinity. The purpose is to verify the TKE budget estimates and the prediction that thermobaricity should cause a mid-depth maximum in TKE.

LES Model of Deep Free Convection

75x75 horizontal grid   25 vertical levels

Q = 200 w/m^2

3600 m
$\Delta x = \Delta y = 48$ m

3600 m
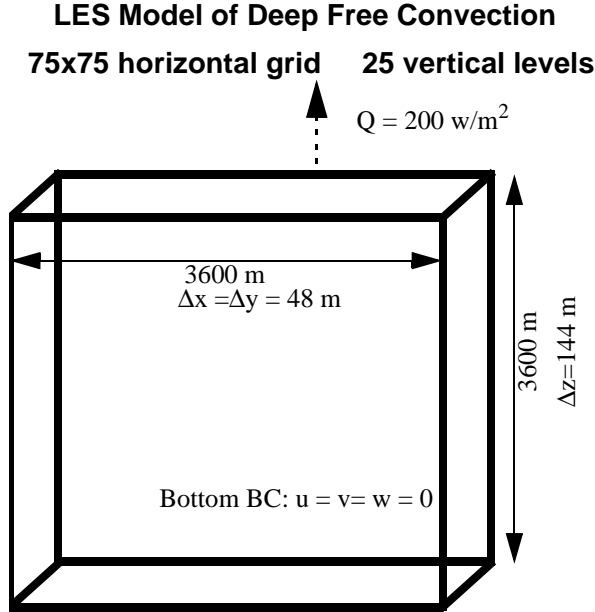$\Delta z = 144$ m

Bottom BC: u = v= w = 0

Fig. 3. Schematic diagram of LES model for first numerical experiment.

For the purely thermal convection in this first numerical experiment, the model domain is cubical, with each side 3.6 km, with periodic lateral boundary conditions (see Figure 3). The ocean was assumed initially quiescent and homogeneous with the surface temperature at -1.8 C, just above freezing and typical of the western Greenland gyre during winter. Convection was initiated with application of a constant upward surface heat flux of 200 watts/m^2. With no wind stress in these free convection experiments, a slip condition was prescribed for the surface velocity, allowing the surface temperature field to be freely advected

by the buoyancy-driven convection. Without an underlying salinity stratification, there was no loss of TKE to entrainment damping or to radiating internal waves. The simulation was continued for several days, until turbulence filled the model domain and a statistical equilibrium was approximated.

Figure 4 shows representative instantaneous horizontal averages of both the turbulent buoyancy flux and the sub-grid scale conductive buoyancy flux versus depth after a statistical steady state was reached. Thermobaricity causes the turbulent buoyancy flux to be greatest near the 2500-m depth. The peak buoyancy flux in Figure 4 exceeds that predicted in Figure 1 because of the unsteadiness in the LES plume field and because individual large plumes can penetrate to depth without being significantly dissipated. The buoyancy flux profile in Figure 4 was during one of these plume events. The subgrid-scale conductive buoyancy flux also shown is considerably smaller in magnitude than the resolved flux, indicating that the energetics of the large eddies are independent of the subgrid-scale parameterization.
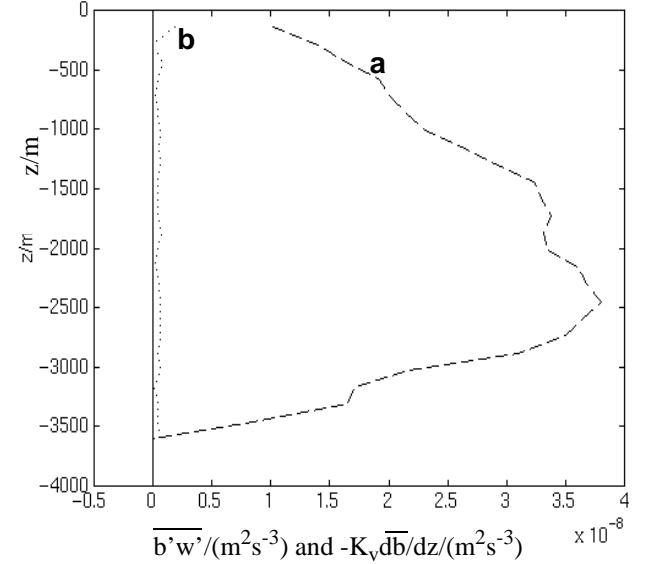
Fig. 4. Vertical profiles of horizontally-averaged buoyancy fluxes versus depth for (a) resolved turbulent motion (dashed), and (b) subgrid-scale diffusion (dotted). Averages are over the x-y domain of (3.6 km)^2 and computed for an arbitrary time during the fifth day after model initiation when the convective turbulence has achieved an approximate statistical equilibrium.

Figure 5 confirms the expectation of a maximum vertical TKE near mid-depth, with peak root-mean-square vertical velocities of about 3 cm/sec. Near the 2000-m depth there is a broad maximum in the total TKE, with $\overline{u^2 + v^2 + w^2}$ =3.2x10^{-3}m^2/s^2. There is also a peak in the horizontal TKE at the surface because of rotation and inertial effects. Turbulent transport and pressure redistribution

together tend to reduce local maxima in total TKE and in each of the components.
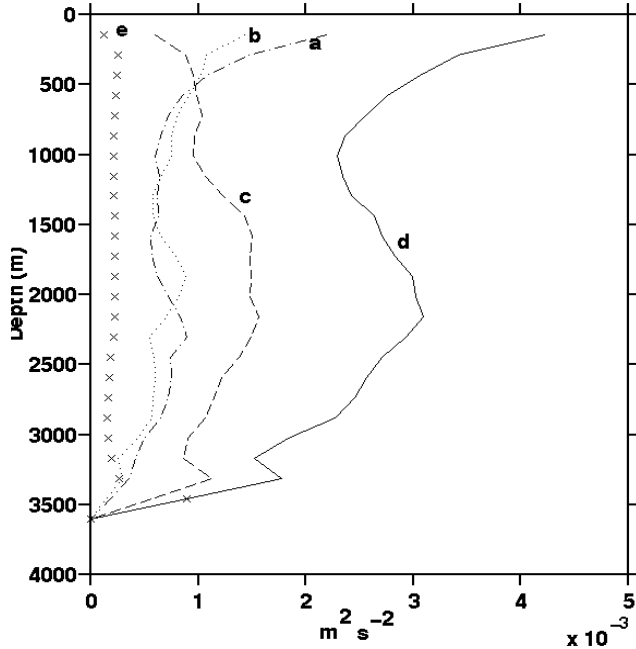

Fig. 5. For the same period as for Figure 4, vertical profiles of horizontally-averaged values of TKE components: (a) $\overline{u^2}$, (b) $\overline{v^2}$, (c) $\overline{w^2}$, (d) total TKE, and (e) subgrid TKE.

The structure of the convective elements throughout the three-dimensional model domain has been studied by Garwood [1993] using hundreds of vertical and horizontal sections of contoured temperature together with time series of parcel trajectories. Video recording of time series of these sections showed that the longevity of vertical plumes seldom exceeds the time for a parcel of surface-cooled water to sink to the bottom. Because of the intensity of the three-dimensional vorticity, the loss of energy from the largest plumes to smaller eddies prevents the most energetic vertical plumes from lasting much longer than several hours, or the integral time scale for the turbulence. The effects of thermobaricity are evident in Plate 1a, with the lower portions of downward-accelerating plumes appearing to pull away.

Horizontal sections showing the temperature field have a considerable degree of organization. See Plate 1b. Particularly noteworthy are the organized mesoscale features that somewhat resemble Rayleigh-Benard cells [Carsey and Garwood, 1993]. Unlike Rayleigh-Benard cells, however, these are nonstationary cells that are influenced by both planetary rotation and the smaller-scale three-dimensional turbulent vortices.

The large cells with 3-6 sides are warmer (red) than the cold (blue) areas of the field, by about 0.02 C. The largest cells are divergent and rotate anticyclonically. These warmer regions are fed by rising water that diverges at the surface and begins to spin under the influence of Coriolis. With a maximum horizontal speed of about 0.06 m/sec and a horizontal scale size (D) of about 1 km, the largest cells have a local Rossby number (Ro=w*/fD) of about 0.5.

The coldest near-surface water lies in linear convergence lines between the expanding warm cells and has a large cyclonic vorticity that is accentuated by the vertical stretching induced by sinking. The local Rossby number of the sinking plumes is therefore much greater than unity.

Carsey and Garwood [1993] believe that they see similar surface features to those predicted by the LES in ERS-1 SAR data from the Greenland Sea during the winter. A functional relationship was suggested between the horizontal scale size (D) of the mesoscale features seen at the surface and the interior state of the ocean and surface forcing: the depth of mixing, h, the thermobaric depth, H_α, and the free and forced convection velocities, w* and $u*=\tau^{0.5}$, where τ is the wind stress. For a statistical steady state, this function should have the form,

$$D/h = \Phi[Ro, h/H_\alpha, w*/u*] \qquad (18)$$

The function Φ needs to be evaluated from future observations, both in situ and remote, together with model simulations. Then Q_0, τ, and h could potentially be diagnosed from satellite observations alone.

3. THERMOBARIC CONDITIONAL INSTABILITIES

Thermobaric effects in the presence of salinity stratification are now considered. For typical polar sea conditions near freezing, the surface value of the thermal expansion coefficient is $\alpha_0 = 2.75 \times 10^{-5} C^{-1}$, the thermobaric depth defined by (2) is H_α=990 m, and the salinity contraction coefficient, β=0.791x10^{-3}psu^{-1}, is nearly depth independent. Under these conditions, the magnitude of the buoyancy attributable to temperature differences increases a little over 0.1% with each meter of downward displacement, while the buoyancy attributable to salinity differences remains constant. In other words, if two parcels of equal density in the mixed layer that have different θ-S properties are displaced downward together, the colder and fresher parcel will be compressed more than the warmer and more saline parcel.

An upside-down physical analog to cumulus convection that may occur in polar seas due to the combined effects of salinity and temperature stratification in the nonlinear equation of state is hypothesized [Garwood, 1992a,b]. In the thermodynamic analog, the halocline plays the same stabilizing role in the polar seas as does the potential tem-

perature profile in the tropical atmosphere, and low oceanic mixed layer temperature plays a similar destabilizing role as high humidity in the marine atmospheric boundary layer.

Perhaps the simplest case that may lead to a thermobaric conditional instability is a two-layer system with a surface mixed layer of colder and fresher water overlying a deeper layer that is both more saline and warmer than the mixed layer. If mixed layer water is displaced a short distance downward into the deeper layer, it will be buoyant and lifted back to the interface. However, analogous to the release of latent heat by a rising parcel of air from the marine atmospheric surface layer, the increase in thermal expansion coefficient with depth may make temperature differences overcome salinity differences in determining buoyancy if the ocean mixed layer parcel is displaced to sufficient depth and differentially compressed by high pressure. So, if a mixed layer parcel or the interface itself is given sufficient downward motion by turbulence or internal waves, then the displaced water may become more dense than the ambient deeper water, with buoyancy not conserved. Parcels or plumes could then break away from the interface and be accelerated downward through the deeper layer. If the deeper layer is itself nonturbulent, such downward moving parcels or plumes may be convected to the bottom, or until they reach water of greater in situ density, without appreciable mixing with the intermediate water.

A critical depth (h_{cr}) is predicted for the thermobaric instability to occur,

$$h_{cr} = (\beta \Delta S / \alpha_0 \Delta \theta - 1)H_\alpha \qquad (19)$$

where ΔS and $\Delta \theta$ are the increases in salinity and potential temperature for the underlying layer relative to the surface mixed layer. The critical condition (19) applies to vertical displacement, but is similar in form to Aagaard et al.'s [1985] critical pressure level applied to horizontal interleaving of water masses.

3.1. Parcel Instability Criterion and Large-Eddy Simulation

An increase in h above h_{cr} due to entrainment is predicted by mixed layer entrainment models in response to either force convection by wind stress and/or free convection driven by surface heat flux with or without freezing. However, parcels of negatively buoyant water in such a convective turbulent boundary layer may not be confined to the mixed layer, with their energy used only for dissipation and entrainment at the base of the mixed layer.

A parcel of surface-cooled water will accelerate downward until it meets the underlying more saline and warmer water. Upon entering the pycnocline, the parcel will at first

be positively buoyant, slowing its penetration. If the parcel's initial downward speed is small, it may return to the mixed layer. However, if the initial downward speed is large enough, the parcel may pass below the critical depth before its downward speed is lost, and a parcel instability should occur. The parcel will then fall until it meets the bottom or another layer of greater density, or until it is diffused by turbulent mixing. As an example, if $H_\alpha = 904$ m, and the magnitude of the stratification due to salinity exceeds by 24% the magnitude of the compensating stratification due to temperature, then the critical depth would be (1.24-1)x(904 m), or 217 m. If the mixed layer depth were 200 m, then a plume of mixed layer water that penetrated more than 17 m into the lower layer would initiate a parcel instability. Of course, partial mixing between the parcel and the surrounding water will influence these tendencies, but the basic premise is expected to apply because the water column being penetrated is not expected to be turbulent and mixing should be minimized.
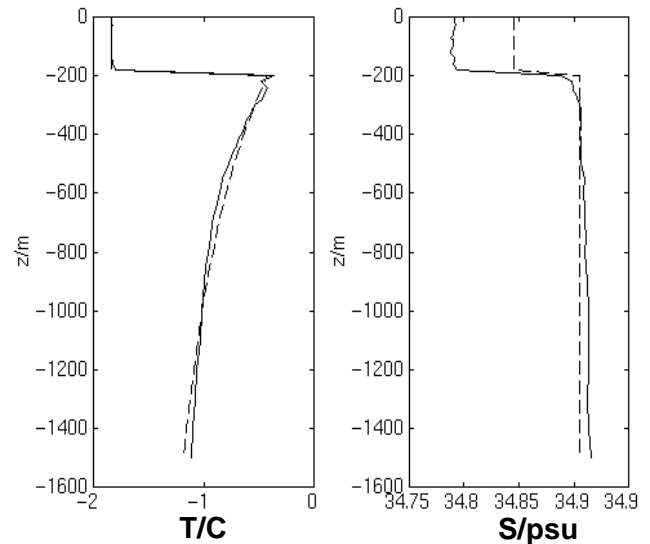

Fig. 6. Representative western Greenland Sea wintertime temperature and salinity profiles, from observations by Quadfasel and Ungewiβ [1988] (solid curves). Dashed curves are hypothetical profiles that approximate the change in the observations that would accompany a mixed layer salinity increase associated with the freezing of 25 cm of surface water.

Figure 6 from observations by Quadfasel and Ungewiβ [1988] shows that the lower layer of such a system need not be homogeneous. It may be stably stratified. The dashed profiles are for a neutral parcel: if a parcel of mixed layer water is displaced vertically into the lower layer, it will have identical buoyancy to the surrounding water regardless of depth. The thermal expansion increase with depth exactly compensates the in situ temperature gradient. As can be seen, only a minor increase in surface salinity, equivalent to freezing 25 cm of water, will make the water column susceptible to parcel instability, poten-

tially allowing penetrative convection events deep into the thermocline without a concomitant mixing of the thermocline. In observations during the following winter, Rudels et al. [1989] observed such a narrow "pipe," with vertical penetration at a single site to 1250 m, while the surrounding deep water remained unmixed. Although Rudels et al. suggest a double-diffusion mechanism for the density anomaly to develop, we suggest the parcel instability mechanism. However, what initiates the parcel displacement?

If the initial conditions for a parcel ejected from a mixed layer of thickness h are $\frac{\partial}{\partial t} z|_{t=0} = -w_0$ and $z|_{t=0} = -h$, then the subsequent vertical displacement of the parcel can be predicted from the vertical momentum balance. For the period during which the detrained parcel is contained within the underlying layer, $z < -h$, the acceleration of the parcel is balanced approximately by its buoyancy,

$$\frac{d^2z}{dt^2} = \beta g \Delta S - \alpha_0 g \Delta \theta \left(1 - \frac{z}{H_\alpha}\right) \qquad (20)$$

where g=9.83 m/sec^2 is gravity. Using (19) the solution to (20) may be written as

$$z(t) = -h_{cr} + 0.5C_1 \exp\left[\left(\frac{\alpha_0 g \Delta \theta}{H_\alpha}\right)^{0.5} t\right]$$

$$+ 0.5C_2 \exp\left[-\left(\frac{\alpha_0 g \Delta \theta}{H_\alpha}\right)^{0.5} t\right] \qquad (21)$$

where $\qquad C_1 = h_{cr} - h - w_0 \left(\frac{H_\alpha}{\alpha_0 g \Delta \theta}\right)^{0.5} \qquad$ and

$$C_2 = h_{cr} - h + w_0 \left(\frac{H_\alpha}{\alpha_0 g \Delta \theta}\right)^{0.5}$$

Evaluating (21) as t approaches infinity, and requiring z to approach the critical depth gives the critical initial parcel speed w_0 to be

$$w_{cr} = (h_{cr} - h)\left(\frac{\alpha_0 g \Delta \theta}{H_\alpha}\right)^{0.5} \qquad (22)$$

If the initial parcel speed is assumed to be provided by mixed layer free convection so that $w_0 = w^*$, then (17) and

(22) may be combined to predict the minimum necessary surface heat flux to give a parcel instability,

$$Q_0 > 2\rho C_p \frac{(h_{cr} - h)^3}{h\left(1 + \frac{h}{3H_\alpha}\right)} (\alpha_0 g)^{0.5} \left(\frac{\Delta \theta}{H_\alpha}\right)^{1.5} \qquad (23)$$

The dashed profiles of Figure 6 provide an example. With $\Delta\theta$=1.50 C, ΔS=0.0636 psu, and h=200 m, (19) gives h_{cr}=217.5 m. Then (23) predicts that $Q_0 > 200$ watts/m^2 would lead to a parcel instability by causing a large enough initial velocity of $w_0 > w_{cr}$=0.011 m/sec to carry incident mixed layer parcels below the critical depth.

An LES numerical experiment was initiated with these values for h, $\Delta\theta$ and ΔS and forced by $Q_0 = 200$ watts/m^2. Plate 2 illustrates a sequence of x-z sections from the LES model. Four hours after initializing the numerical experiment from an initially quiescent and stable ocean, the density interface near $z = -200$ m was deformed and experienced some entrainment mixing. The first parcel instability to break through the interface and continue below the critical depth occurred some 5 hours after initialization. In the second picture in Plate 2, an 80-m wide pipe of mixed layer water has penetrated the lower layer below the critical depth shortly before the simulation was terminated.

3.2. Layer Instability Criterion: Possible Explanation for Scott and Killworth Chimneys

While mixed layer turbulence may provide the initial energy to generate a parcel instability, downwelling by the larger-scale circulation may lead to a related instability. If h is made to exceed h_{cr} in (19), either by Ekman pumping or other downwelling process, then the entire upper layer will become hydrostatically unstable, and a layer instability may occur. Such may have been the case for the chimney features having a 2-3 km width reported by Scott and Killworth [1991]. Although there were no local salinity measurements for verification in Scott and Killworth's observations, an originally hydrostatically stable layer with stable vertical gradients, $(\partial S / \partial z)/(\partial \theta / \partial z) > \alpha/\beta$, could have been made unstable if advected below a critical depth,

$$z_{cr} = -\left(\frac{\beta}{\alpha_0} \frac{\partial S}{\partial \theta} - 1\right) H_\alpha \quad . \qquad (24)$$

Thus (24) is a generalization of the critical depth defined by (19) and applies to both stratified and well-mixed layers. In any case, advection of a layer with vertical temperature and salinity gradients below z_{cr} could conceivably

lead to the draining of either a surface or an intermediate layer down a pipe created in the region that was advected below the critical depth.

4. CONCLUSIONS AND FUTURE NUMERICAL INVESTIGATION

Numerical simulations of thermobaric convection appear to verify two earlier hypotheses:

- There is a mid-depth maximum in the total TKE for three-dimensional simulations of deep thermally-driven free convection in the polar seas.

- A conditional instability thermodynamically similar to atmospheric cumulus convection can occur for the right combination of cold mixed layer water overlying warmer more saline water. A parcel instability was numerically simulated for representative winter polar-sea conditions, but many oceanic conditional instabilities may also be of the layer-type.

The numerical solutions revealed details of the thermobaric convection that had not been anticipated:

- The most observable aspect of the surface during free convection may be the "ragged-net" field of larger cells of rising warmer water separated by linear shear zones of colder sinking water, as reported by Carsey and Garwood [1993]. Remote sensing of this surface manifestation of convection may be used potentially to diagnose the state of the ocean interior as well as the surface forcing.

- With regard to the vertical structure, the sinking plumes of colder water may be separated into discontinuous parcels because of the greater downward acceleration of the leading edge of the plumes directly attributable to thermobaricity and also because of convective interaction between the larger plumes and the more isotropic but intense smaller-scale turbulence.

Additional numerical experiments are required to answer key questions:

- How dissipative are the convection cells?

- How important is the tendency to conserve entropy [Garwood and Isakari, 1993] and not mix the intermediate water column that is penetrated by plumes that extend deep into the intermediate waters and possibly to the bottom?

- Finally, LES computations may guide parameterization of both deep mixed layer dynamics and sub-grid scale penetrative convection. A major goal is to include the effects of deep convection in ocean circulation models without having to resolve the plumes themselves.

## 5. REFERENCES

Aagaard, K., J. H. Swift, and D. C. Carmack, Thermohaline circulation in the Arctic Mediterranean Seas, *J. Geophys. Res.*, 90, 4833-4846, 1985.

Brugge, R., H. L. Jones, and J. C. Marshall, Non-hydrostatic ocean modeling for studies of open-ocean deep convection, In *Deep Convection and Deep Water Formation in the Oceans*, Ed. by P. C. Chu and J. C. Gascard, 325-340, 1991.

Carmack, E. C., and D. M. Farmer, Cooling processes in deep, temperate lakes: A review with examples from two lakes in British Columbia, *J. Mar. Res.*, 40, Supp., 85-111, 1982.

Carsey, F. D. and R. W. Garwood, Jr., Identification of modeled ocean plumes in Greenland Gyre ERS-1 SAR data, *Geophys. Res. Lett.*, 20, 2207-2210, 1993.

Farmer, D. M., and E. C. Carmack, Wind mixing and restratification in a lake near the temperature of maximum density, *J. Phys. Oceanogr.*, 11, 1516-1533.

Fox, D. G., and S. A. Orszag, Pseudospectral approximation to two-dimensional turbulence, *J. Comput. Phys.*, 11, 612-619, 1973.

Gallacher, P. C., Large eddy simulation of the turbulent boundary layer in the upper ocean (abstract), *Trans. Am. Geophys. Union,* 71, 1354, 1990.

Garwood, R. W., Jr., Enhancements to deep turbulent entrainment, In *Deep Convection and Deep Water Formation in the Oceans,* Ed. by P. C. Chu and J. C. Gascard, 197-213, 1991.

Garwood, R. W., Jr., Missing physics for deep convection? Arctic System Science Ocean-Atmosphere-Ice Interactions Modeling Workshop, Pacific Grove, Report No. 1, 49-54, 1992a.

Garwood, R. W., Jr., Oceanic convective instabilities hypothesized, *ARCSS-OAII Newsletter,* 2, 4-5, 1992b.

Garwood, R. W., Jr., Parcel and layer instability convection, Nansen Centennial Symposium, Solstrand-Bergen, Norway, 21-25 June 1993.

Garwood, R. W., and S. M. Isakari, Entropy Conserving deep convection in the Weddell Sea, *Proceedings* Fourth International Conf. Southern Hemisphere Meteorol. and Oceanogr., Hobart, 29 March - 2 April, 503-504, 1993.

Gill, A. E., Circulation and bottom water formation in the Weddell Sea, *Deep-Sea Res.*, 20,111-140, 1973.

Gordon, A. L., Deep Antarctic convection west of Maud Rise, *J. Phys. Oceanogr.*, 8, 600-612, 1978.

Holton, J. R., *An Introduction To Dynamic Meteorology,* Academic Press, New York, 1972.

Jones, H. and J. Marshall, Convection with rotation in a neutral ocean: A study of open-ocean deep convection, *J. Phys. Oceanogr.*, 23, 1009-1039, 1993.

Killworth, P. D., On "chimney" formations in the deep ocean, *J. Phys. Oceanogr.*, 9, 531-554, 1979.

Lemke, P., A coupled one-dimensional sea ice model, *J. Geophys. Res.*, 92, 13164-13172, 1987.

Martinson, D. G., Evolution of the southern ocean winter mixed layer and sea ice: Open ocean deepwater formation and ventilation, *J. Geophys. Res.*, 95, 11641-11654, 1990.

McDougall, T. J., The relative roles of diapycnal and isopycnal mixing on subsurface watermass conversion, *J. Phys. Oceanogr.*, 14, 1577-1589, 1984.

McWilliams, J. C., P. C. Gallacher, C.-H. Moeng, and J. C. Wyngaard, Modeling the oceanic planetary boundary layer, in *Large Eddy Simulation of Complex Engineering and Geophysical Flows*, Cambridge University Press, in press, 1992.

Moeng, C.-H., A large-eddy simulation model for the study of planetary boundary layer problems, *J. Atmos. Sci.*, 41, 2052-2062, 1984.

Moeng, C.-H., and J. C. Wyngaard, Spectral analysis of large-eddy simulations of the convective boundary layer, *J. Atmos. Sci.*, 45, 3573-3587, 1988.

Quadfasel, D. and M. Ungewiβ, MIZEX 87 - RV Valdivia Cruise 54, CTD Observations in the Greenland Sea, *Technical Report 5-88*, Institut fur Meereskunde der Universitat Hamburg, 1988.

Rudels, B., D. Quadfasel, H. Friedrich, and M.-N. Houssais, Greenland Sea convection in the winter of 1987-1988, *J. Geophys. Res.*, 94, 3223-3227,1989.

Schott, F., M. Visbeck and J. Fischer, Observations of vertical currents and convection in the central Greenland Sea during the winter of 1988-1989, *J. Geophys. Res.,* 98, 14401-14422, 1993.

Scott, J. C. and P. D. Killworth, Upper ocean structures in the southwestern Iceland Sea: A preliminary report, In *Deep Convection and Deep Water Formation in the Oceans*, Ed. by P. C. Chu and J. C. Gascard, 107-122, 1991.

Smagorinsky, J., General circulation experiments with the primitive equations, *Mon. Wea. Rev.*, 91, 99-165, 1963.

———————————————

R. W. Garwood, Jr. and S. M. Isakari, Department of Oceanography, Naval Postgraduate School, Code OC/Gd, Monterey, Ca 93943, USA.

P. C. Gallacher, Naval Research Laboratory, Stennis Space Center, MS 39529, USA.
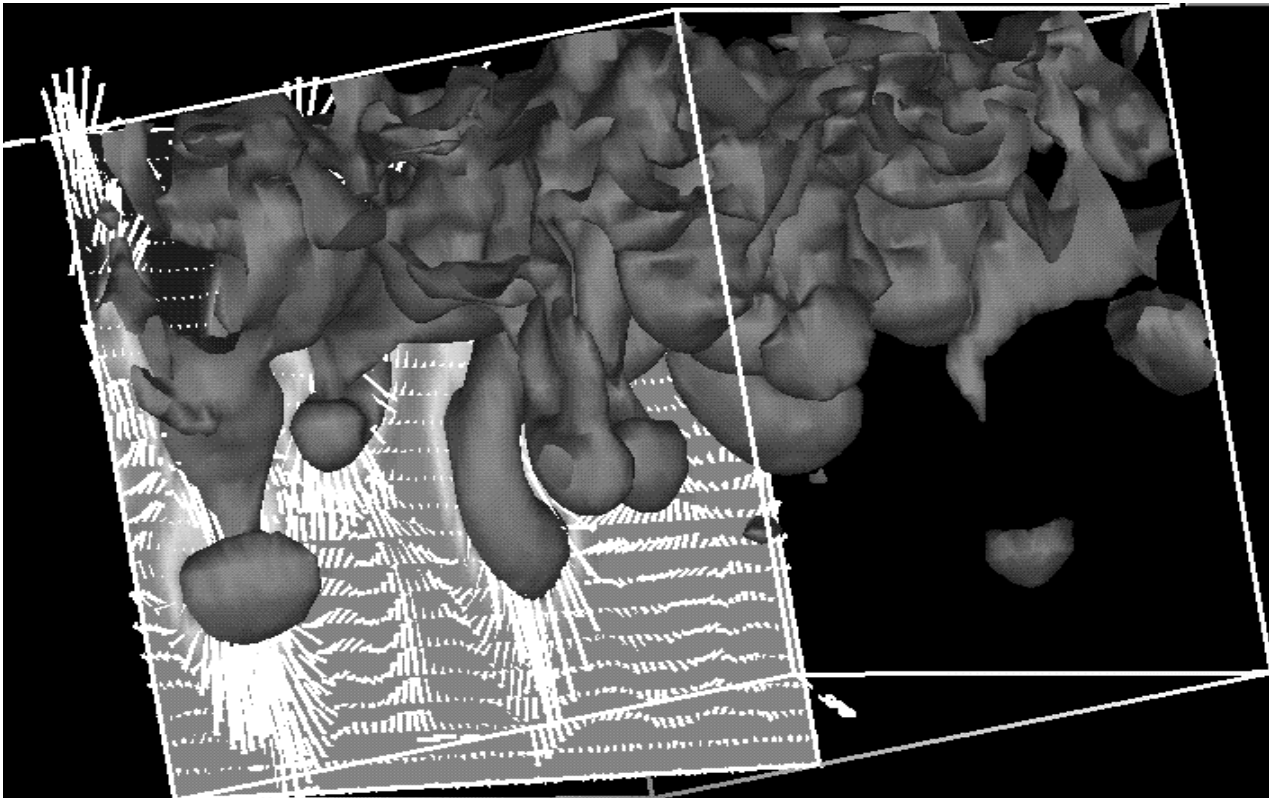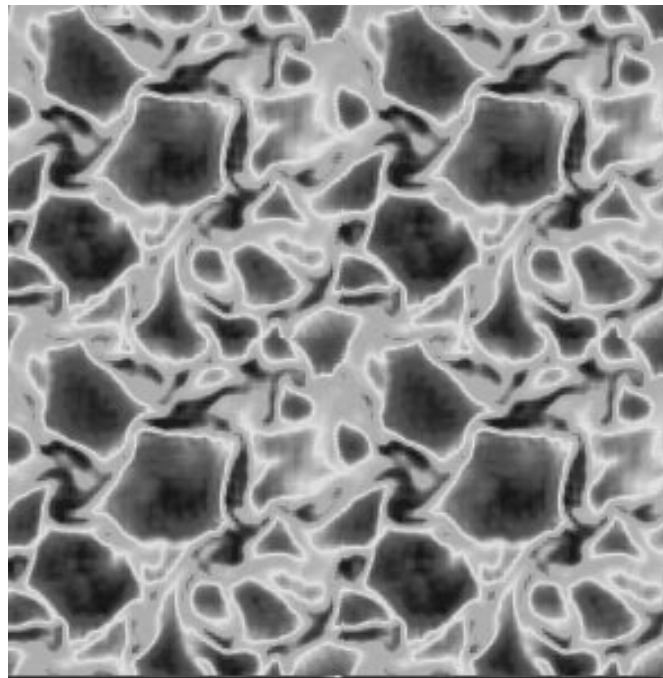
Plate 1. First LES experiment with thermal free convection only, 1.25 days after initiation of an upward surface heat flux of 200 watts/ m^2. (a) Three-dimensional depiction of constant-temperature surfaces in a 3.6-km cube. Blue is -1.806 C, and green is -1.002 C. (b) Cellular mesoscale convection cells predicted for the surface temperature field. Area shown is 7.2 km x 7.2 km. Cyclical horizontal boundary conditions enable the depicted area to be expanded four-fold for visual effect.
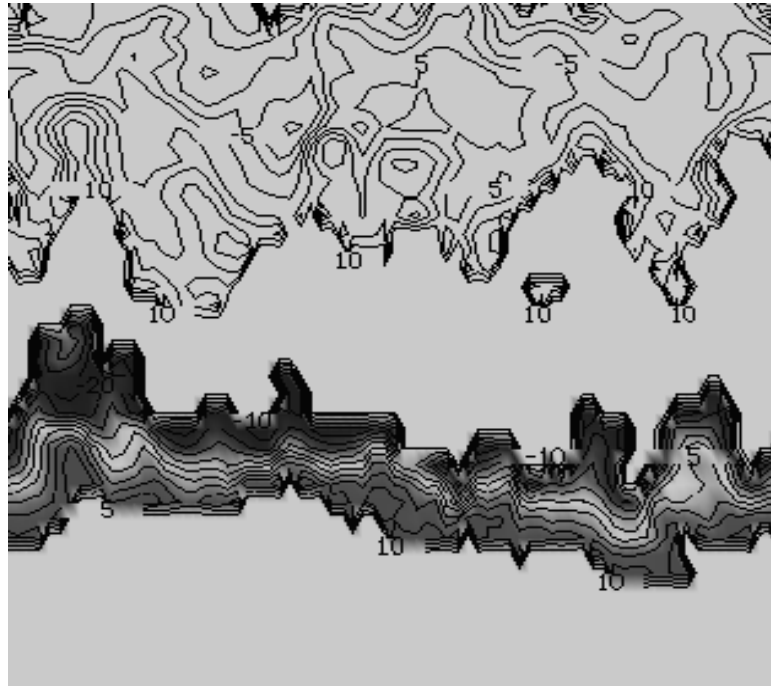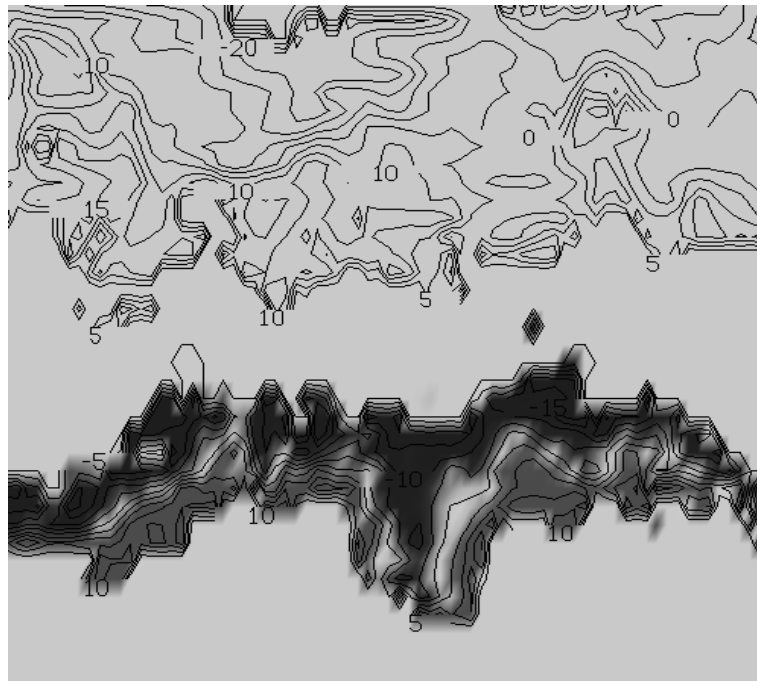
a

b

Plate 2. Second LES experiment including salinity stratification, (a) 4 hours, and (b) 5 hours after initiation of surface cooling. Parcel instability occurs in the second of these two sequential vertical temperature sections. The first section shows significant interface deformation by mixed layer turbulence. The second picture shows the onset of the parcel instability with an 80-m wide plume penetrating the pycnocline. Contours of relative temperature in the upper 100 m are in millidegrees, and contours of relative temperature near the interface at z=-200 m are in centidegrees.